Design to Improve Thrust Force Performance of Dual-side Primary Permanent-magnet Vernier Linear Motor*

Jinghua Ji [1], *Xuhui Zhu*[2], *Hongyu Tang*[3], *Liang Xu*[1] *and Wenxiang Zhao*[1*]

(1. School of Electrical and Information Engineering, Jiangsu University, Zhenjiang 212013, China;
2. School of Electrical Engineering, Nantong University, Nantong 226019, China;
3. School of Electrical and Information, Zhenjiang College, Zhenjiang 212028, China)

Abstract: A novel dual-side primary permanent-magnet vernier linear (DS-PPMVL) motors is proposed. The novelty of the proposed motors is the design of asymmetric consequent poles on the mover, which can effectively enforce the flux-modulation effect and improve the thrust force performance. First, the topologies and operation principle are introduced. Subsequently, the structure relationships between the existing and proposed motors are discussed. Then, a unified analytical model is built. Accordingly, the magnetic field generated by the consequent pole is calculated. Meanwhile, the performance improvement mechanism with the asymmetric consequent pole is analyzed. To improve the efficiency of motor optimization, multi-objective optimization method is adopted to obtain the global optimal solution combination of structure parameters. The proposed motors exhibit higher thrust force, higher force density, less PM consumption, and better overload performance than the existing DS-PPMVL motor. Finally, experiments are conducted based on the existing prototype to verify the accuracy of the design and analysis.

Keywords: Consequent pole, dual-side motor, flux modulation, linear motor, primary permanent-magnet

1 Introduction

Owing to the output power in the form of linear motion, linear motors exhibit remarkable application prospects in urban transit [1] and energy conversion systems [2]. Compared to conventional induction linear motors, permanent-magnet (PM) linear motors exhibit significant advantages in thrust force performance and efficiency. Among them, primary PM linear (PPML) motors have garnered significant attention for their low cost when adopted in long-stroke applications [3]. For PPML motors, the windings and PMs are relatively static because they are both placed on the primary side, while the secondary side solely comprises the salient pole. Therefore, the operation principle of the PPML motor is based on the flux-modulation principle, which significantly differs from the conventional motor principle [4-5].

The dual-side primary PM vernier linear (DS-PPMVL) motor can offer better thrust force performance than single-side alternatives [6]. In Ref. [7], a DS-PPMVL motor was proposed, which combines the advantages of simple structure, strong robustness, high thrust force density, and high efficiency. However, compared with the conventional induction motor, this DS-PPMVL motor consumes more PM material, exhibits prominent contradiction in primary space, and eliminates defects in power factor and overload performances. In Ref. [8], a DS-PPMVL motor with PMs and windings separately placed on two relatively static primaries was proposed. The space contradiction between PMs and windings can be addressed. Therefore, the electromagnetic load can be increased to improve performance. However, it also exhibits a defect in power factor. To improve the power factor, a DS-PPMVL motor was proposed in Ref. [9]. The

Manuscript received December 27, 2021; revised March 15, 2022; accepted March 23, 2022. Date of publication June 30, 2023; date of current version October 22, 2022.
* Corresponding Author, E-mail: zwx@ujs.edu.cn
* Supported in part by the National Natural Science Foundation of China under Grant 51977099, and in part by the Natural Science Foundation of Jiangsu Province under Grant BK20191225.
Digital Object Identifier: 10.23919/CJEE.2023.000005

PMs are inserted in the yoke of the primary (namely mover). The flux linkage can form an effective loop among two secondary sides and a primary side, which can reduce the flux leakage and improve the power factor. Based on the multi-objective optimization technique, the power factor of the motor can reach up to 0.945 [10]. Nevertheless, the contradiction between the slot area and PM triggers the low thrust force density and poor overload capability.

In addition, it is important to improve the PM utilization ratio in industrial application for its high cost. Meanwhile, reducing the consumption of PM is also beneficial in minimizing the saturation degree and improving the overload capability of the motor. Adopting the consequent pole (CP) is an effective approach to reducing the consumption of PM while ensuring the output capacity of the motor [11-13]. In Ref. [14], a CP flux-reversal motor was analyzed based on the flux-modulation theory. Compared to the conventional flux-reversal motor, the proposed motor has merits in back electromotive force (back-EMF) and torque. Furthermore, a CP PM structure with a magnetic focusing effect is applied to flux switching the PM motor in Ref. [15]. Accordingly, the performances of the motor can be significantly improved.

This paper proposes the application of a CP PM structure to the DS-PPMVL motor to improve the thrust force performance. The topologies and operation principle of the proposed motors are discussed in Section 2. In Section 3, the structure relationships between the existing and proposed motors are clarified. Furthermore, the unified analytical model and performance improvement mechanism of the proposed motors are discussed. In addition, the adoption of the multi-objective optimization method to obtain the optimum combination of structure parameters is described in Section 4. Compared to conventional optimization processes, this method can significantly improve the efficiency of motor optimization. Based on the optimization results, the electromagnetic performance of the proposed motors can be predicted using the finite element method (FEM). The performance comparisons between the proposed motors and the existing motor is presented in Section 5. Finally, the experiments on the existing prototype are described in Section 6. The results verify the accuracy of the motor design and analysis.

2 Configurations and operation principle

2.1 Configurations

Fig. 1 compares the topologies of the proposed DS-PPMVL and existing motors. These motors share the similar salient teeth in the stator. Meanwhile, windings and PMs are all positioned in the mover. The difference is that the salient teeth of the proposed motor I are faced with each other, while those in the existing motor and proposed motor II are staggered half of the pitch of the stator salient teeth. In addition, the CP PMs are placed on the top of the armature teeth in motor I, while they are placed on the opening of armature slots in motor II. Unlike the proposed motors, the PMs are inserted in the yoke of the mover in the existing motor. In addition, taking the proposed motor I as an example, a few important design dimensions and their definitions are illustrated in Fig. 2.

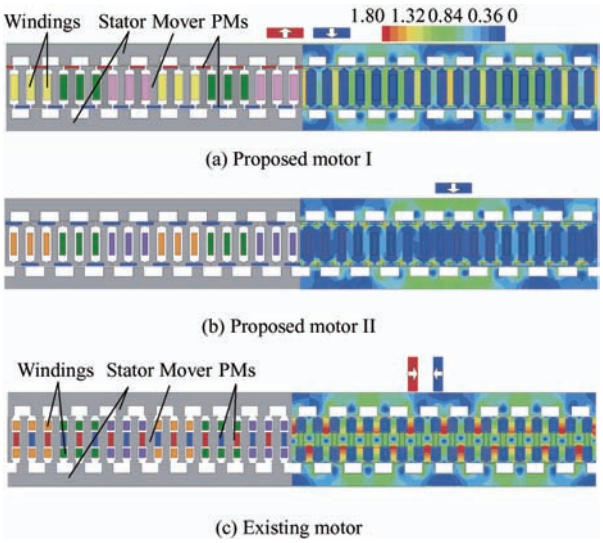

Fig. 1 Structures of DS-PPMVL motors

In addition, it is necessary to point out the difference of the PM magnetization direction. For the existing motor, the magnetization direction of the PMs is parallel to the motion direction of the mover, and that of the two adjacent PMs is opposite. For the proposed motors, the magnetization direction of PMs is perpendicular to the motion direction of the mover. The magnetization direction of PMs on the adjacent armature teeth of the proposed motor I is opposite, while that of the proposed motor II is the same.

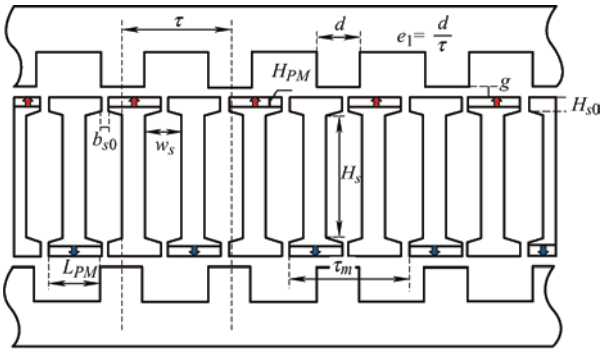

τ: Pole pitch of stator
d: Tooth width of stator
H_{PM}: Thickness of PM
g: Length of air-gap
b_{s0}: Opening width of slot
H_s: Height of slot
L_{PM}: Length of PM
τ_m: Pole pitch of mover
w_s: Width of slot
H_{s0}: Height of pole shoe

Fig. 2 Design dimensions

2.2 Operation principle

The operation principle of the DS-PPMVL motor is the flux-modulation effect. For the proposed motors, the initial PM magnetomotive force (MMF) can be expressed as

$$F(x,t)=\sum_{i,odd}F_{i\max}\cos\left[ip_{PM}\frac{2\pi(x-vt)}{l_m}\right] \tag{1}$$

where $F_{i\max}$, p_{PM}, v, and l_m denote the amplitude of the i^{th} MMF harmonic, pole pair of PMs, velocity, and length of the mover, respectively.

For the permeance variation, only the slotting effect of the stator should be considered and it can be expressed as

$$\Lambda(x)=\Lambda_0+\sum_{k=1}^{\infty}\Lambda_0\Lambda_k\cos\left[kZ_s\frac{2\pi}{l_m}(x-x_0)\right] \tag{2}$$

where Λ_0, Λ_k, Z_s, and x_0 represent the DC component of permeance, amplitude of the relative specific permeance harmonic, number of the modulator, and initial position of the stator, respectively.

According to Eqs. (1) and (2), the flux density of the air gap can be expressed as

$$B(x,t)=F(x,t)\Lambda(x)=\underbrace{\sum_{i,odd}F_{i\max}\Lambda_0\cos\left[ip_{PM}\frac{2\pi(x-vt)}{l_m}\right]}_{\text{No-modulated harmonic}}+\underbrace{\frac{1}{2}\sum_{i,odd}\sum_{k=1}^{\infty}F_{i\max}\Lambda_0\Lambda_k\cos\frac{2\pi}{l_m}\left[(ip_{PM}\pm kZ_s)x\pm kZ_sx_0-ip_{PM}vt\right]}_{\text{Modulated harmonic}} \tag{3}$$

The first item represents the no-modulated harmonic, which is generated by the PM MMF and DC component of permeance. The second item is the modulated harmonic, which is generated by the PM MMF and AC component of permeance. Therefore, the harmonic pole pair of air-gap magnetic field can be summarized as

$$p_{i,k}=\left|ip_{PM}\pm kZ_s\right| \quad i=1,3,5,\cdots \quad k=0,1,2,\cdots \tag{4}$$

To improve the thrust force performance, the quantitative relationship among the pole pair numbers of armature winding (p_{PM}), number of modulator, and pole pair number of PM should be satisfied as

$$p_w=\left|Z_s-p_{PM}\right| \tag{5}$$

Meanwhile, the modulation ratio G_r can be defined as

$$G_r=\frac{p_{PM}}{p_w}=\frac{p_{PM}}{\left|Z_s-p_{PM}\right|} \tag{6}$$

3 Structure relationships, analytical model, and performance improvement mechanism

3.1 Structure relationships

The PMs of the existing motor are inserted in the yoke of the mover. For the air gap, the MMF can be considered on the surface of the mover teeth. Therefore, the magnetic source of the existing motor can be considered the surface mounted on the mover. To ensure the air-gap length of the motor, the thickness of the equivalent magnetic source is zero. Meanwhile, the MMF amplitude value of the equivalent magnetic source is related to the magnetization thickness, PM length, and teeth top width. The evolution process is presented in Fig. 3. Evidently, the magnetization direction is opposite the corresponding tooth. In the equivalent model, the yoke of the mover is indispensable; this limits the slot area and eventually affect the motor performance.

To eliminate the influence of the mover yoke, two yokeless DS-PPMVL motors can be obtained by the equivalent model, as illustrated in Fig. 3. For the yokeless motor I, PMs are all surface mounted on top of the mover teeth. The stators are faced with each other. For the yokeless motor II, the PMs are surface mounted on the slot opening. The stators are staggered half of the stator teeth pitch. When the CP PM

structure is applied, the yokeless motor I can be transformed into the proposed motor I, and the yokeless motor II can be transformed into the proposed motor II.

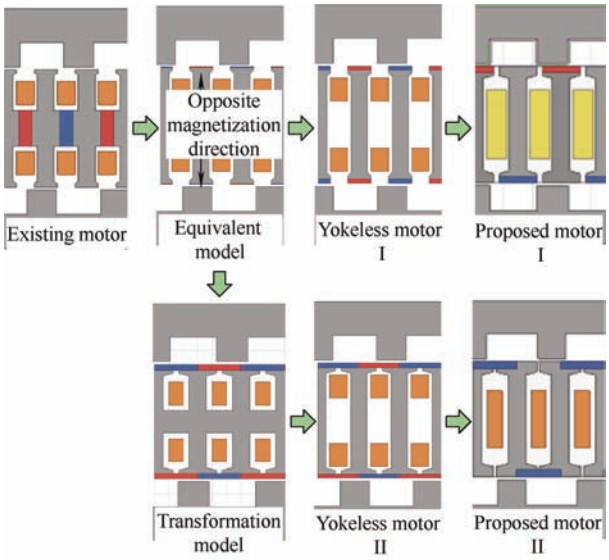

Fig. 3 Evolution processes

3.2 Analytical model

To explain the difference between magnetic fields, a black box model (BBM) is applied to develop the unified analytical model. The saturation effect and end effect are ignored in this part. For the proposed motors and the existing motor, they exhibit similar topology with two secondary cores and one primary sandwiched part. The main difference among the three motors lies in the primary structure. The equivalent models of MMF differ for the different PM arrangements; hence, it is difficult to establish a unified analytical model. In the BBM, the entire primary part can be equivalent to a magnetic source, which can unify the three motors into one equivalent model. Therefore, using BBM is convenient for comparative studies.

First, the magnetic sources are all positioned on the mover. Hence, the mover can be regarded as a black box emitting magnetic field. Second, the effective modulation harmonics of the three motors form a series circuit between the two stators. A stator on one side can be considered as providing a magnetic field path for another one. Therefore, the magnetic field difference of the three motors is primarily triggered by the change in MMF. The unified simplified magnetic field model of the three motors is illustrated by Fig. 4.

The mover can be equivalent to the combination of the magnetic source and its internal reluctance. In addition, the stator can be equivalent to a reluctance function.

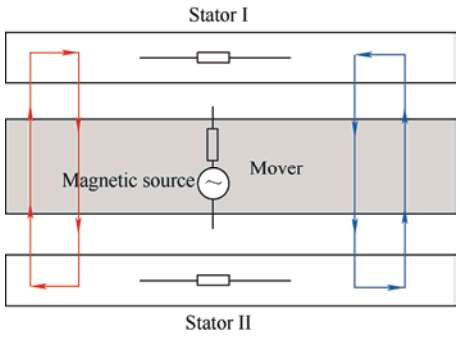

Fig. 4 Unified simplified magnetic field model

Taking the proposed motor I as an example, Fig. 5 presents its equivalent magnetic circuit. The amplitude value of PM MMF can be expressed as

$$F_{PM} = C_F H_{PM} \tag{7}$$

where C_F and H_{PM} are coercive force and magnetization length of PM material, respectively.

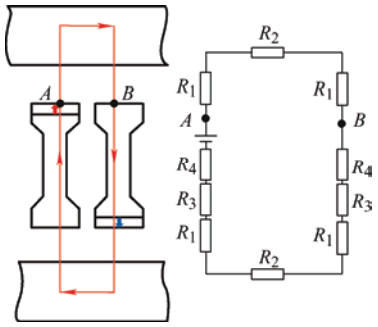

Fig. 5 Equivalent magnetic circuit of the proposed motor I

Therefore, the MMF of points A and B can be expressed as follows

$$\begin{cases} F_A = F_{PM} & A \text{ point} \\ F_B = \dfrac{2R_1+R_2+2R_3+2R_4}{4R_1+2R_2+2R_3+R_4} F_{PM} & B \text{ point} \end{cases} \tag{8}$$

where R_1, R_2, R_3, and R_4 denote the reluctance of air gap, stator iron core, mover iron core, and PM, respectively. The reluctance of the iron core was assumed to be zero in this study. The permeability of PM is equal to that of vacuum. Therefore, R_1, R_2, R_3, and R_4 can be respectively expressed as follows

$$\begin{cases} R_1 = R_g \propto g \\ R_2 = R_3 = 0 \\ R_4 = \dfrac{H_{PM}}{g} R_g \end{cases} \tag{9}$$

Substituting Eqs. (7) and (9) into Eq. (8), the MMF of points A and B can be obtained as

$$\begin{cases} F_A = F_{PM} = C_F H_{PM} \\ F_B = \dfrac{2R_1+2R_4}{4R_1+2R_4} F_{PM} = \dfrac{g+H_{PM}}{2g+H_{PM}} C_F H_{PM} \end{cases} \tag{10}$$

It should be noted that MMF is equal on the surface of the PM, which is also satisfied on the surface of the iron core. Therefore, the MMF waveform of the mover is illustrated in Fig. 6. Via Fourier analysis, the MMF function can be expressed as

$$\begin{cases} F(x,t) = \sum\limits_{n=1,2,\cdots} a_n \cos np_{PM} \dfrac{2\pi(x-vt)}{l_m} \\ a_n = (-1)^{n+1} \dfrac{2\lambda F_{PM}}{n\pi} \sin\left(n\left(1-\dfrac{L_{PM}}{\tau_m}\right)\pi\right) + \\ \qquad (-1)^n \dfrac{(1+\lambda)\tau_m F_{PM}}{n^2\pi^2 b_{s0}} \cos\left(n\dfrac{L_{PM}}{\tau_m}\pi\right) \end{cases} \tag{11}$$

where τ_m and L_{PM} denote the pole pitch of the mover and PM length, respectively. In addition, λ can be defined as

$$\lambda = \frac{g+H_{PM}}{2g+H_{PM}} \tag{12}$$

Meanwhile, the air-gap permeance function of the stator can be expressed as [16]

$$\Lambda_g(x_s, x) = \Lambda_0 \pm \Lambda_1 \cos\left(\frac{2\pi Z_s}{l_m}(x_s - x)\right) \tag{13}$$

where Λ_0 and Λ_1 can be obtained by adopting the conformal mapping method as follows [17]

$$\Lambda_0 = \frac{\mu_0}{g}\left(1 - 1.6\beta\frac{d}{\tau}\right) \tag{14}$$

$$\Lambda_1 = \frac{\mu_0}{g}\frac{2}{\pi}\beta\left[\frac{0.781\,25}{0.781\,25 - 2\left(\dfrac{d}{\tau}\right)^2}\right]\sin\left(1.6\pi\frac{d}{\tau}\right) \tag{15}$$

$$\beta = \frac{1}{2}\left[1 - \frac{1}{\sqrt{1+\left(\dfrac{d}{2g}\right)^2}}\right] \tag{16}$$

where μ_0 denotes the permeability of vacuum. It should be mentioned that the mover permeance is not considered separately, as it has been considered for the distribution of the MMF [18-19].

According to the MMF and permeance, the air gap flux density of the proposed motor I can be expressed as

$$\begin{aligned} B(x,t) = F(x,t)\Lambda(x) = \\ \sum_{n=1,2,\cdots} a_n \Lambda_0 \cos\left[np_{PM}\frac{2\pi(x-vt)}{l_m}\right] + \\ \frac{1}{2}\sum_{n=1,2,\cdots} a_n \Lambda_1 \cos\frac{2\pi}{l_m}\left[\left(np_{PM} - Z_s\right)x - np_{PM}vt + Z_s x_s\right] + \\ \frac{1}{2}\sum_{n=1,2,\cdots} a_n \Lambda_1 \cos\frac{2\pi}{l_m}\left[\left(np_{PM} + Z_s\right)x - np_{PM}vt - Z_s x_s\right] \end{aligned} \tag{17}$$

Therefore, for the proposed motors, the harmonic pole pair of the air-gap magnetic field in Eq. (4) should be revised as

$$p_i = \left|ip_{PM} + Z_s\right| \quad i = 1,2,3,\cdots \tag{18}$$

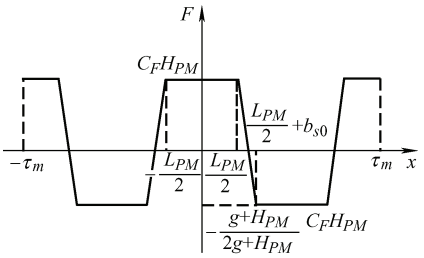

Fig. 6 MMF waveform of the mover

The slotless air-gap flux density waveform and its harmonic analysis of the proposed motor I are presented in Fig. 7. The slotless flux density waveform is revealed to be unsymmetrical. The ratio of the absolute value of the peak to the valley is approximately equal to $1/\lambda$, which agrees well with the results of the analytical model. In addition, even harmonic orders can be generated in air gap by the PMs with CP PM structure.

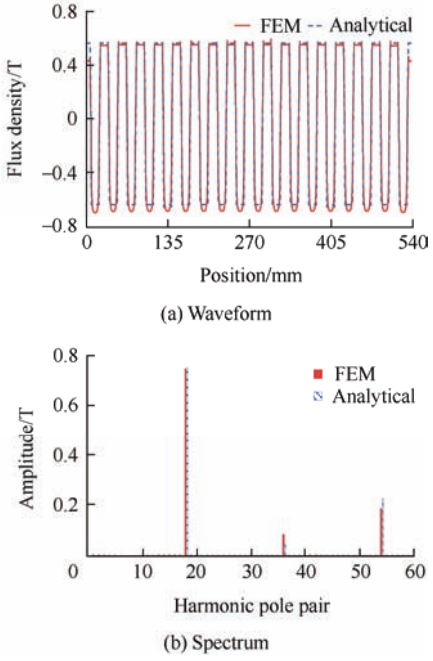

Fig. 7 Slotless flux density of motor I

When stators are slotted, the air-gap flux density of the slotless motor would be modulated by the variation of permeance. Fig. 8 presents the slotted air-gap flux density waveform and its harmonic analysis of the proposed motor I. The obtained results verify the existence of even harmonic orders generated by PMs, and thus verify the correct of the presented analysis. All the results of the analytical method agree well with those calculated by FEM.

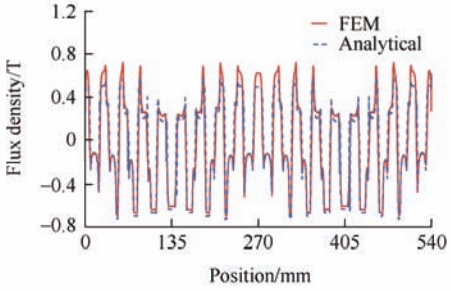

(a) Waveform

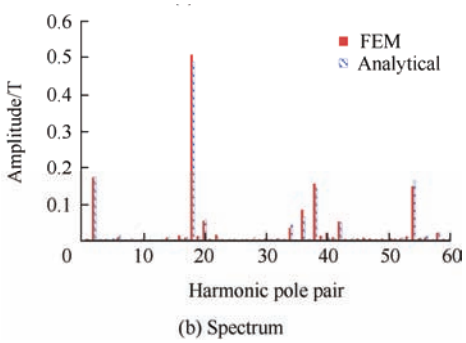

(b) Spectrum

Fig. 8 Slotted flux density of motor I

3.3 Performance improvement mechanism

Under the condition of the same magnetization length of PM, the MMF increment (ΔF_n) is introduced to analyze the performance improvement mechanism. ΔF_n can be expressed as

$$\Delta F_n = \underbrace{C_n}_{\text{First term}} \times \underbrace{\sin\left(\frac{nL_{PM}}{\tau_m}\pi + (-1)^n \arccos\frac{n\pi(\tau_m - 2L_{PM})}{\sqrt{\left[n\pi(\tau_m - 2L_{PM})\right]^2 + (2\tau_m)^2}}\right)}_{\text{Second term}} \tag{19}$$

where

$$\begin{cases} C_n = (\lambda - 1)\dfrac{2F_{PM}}{n\pi}\sqrt{1 + \left(\dfrac{\tau_m}{n\pi b_{s0}}\right)^2} < 0 \\ \tau_m = 2(L_{PM} + b_{s0}) = 15\ \text{mm} \end{cases} \tag{20}$$

Because $\lambda < 1$ in the proposed motors as expressed in Eq. (12), the coefficient of C_n is less than zero. Therefore, the sign of ΔF_n is determined by the second term.

For the flux-modulation motor, the low-order MMF harmonics significantly influence the motor performance. Therefore, only the first-, second-, and third-order MMF harmonics are considered in this study. The variation of the second term with L_{PM} is presented in Fig. 9, where n represents the order of the MMF harmonic. Evidently, when n=1, the value of the second term is almost zero, which implies that the value of the fundamental MMF of the proposed motor I is equal to that of the existing one. The sign of the second term of n=2 is '–' and that of n = 3 is '+,' which implies that the proposed motor I exhibits higher second and lower third MMF harmonics. However, with the increase in L_{PM}, the disadvantage of the third MMF harmonic of the proposed motor I is compensated, and the advantage of the second MMF harmonic is amplified. Therefore, the performance of the proposed motor I can be improved by increasing L_{PM}.

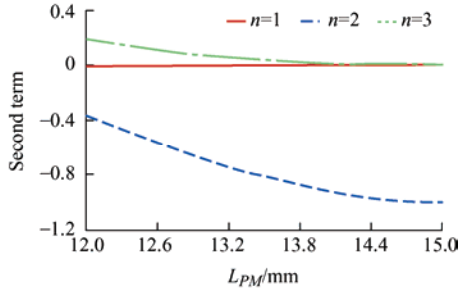

Fig. 9 Second term varies with L_{PM}

4 Motor optimization

For the conventional FEM optimization, the number of samples is the product of the number of optimization parameters, which implies that the optimization requires excessive computing resources and time. In this study, a multi-objective optimization method was adopted to obtain the global optimal solution of the motor. The optimization method is primarily based on the response surface method for its low computational complexity, nonlinear applicability, and high optimization accuracy [10, 20]. The optimization process is illustrated in Fig. 10. It should be point out that the

analytical model is adopted as the base model for motor optimization. Using the model, the sample points were calculated by FEM.

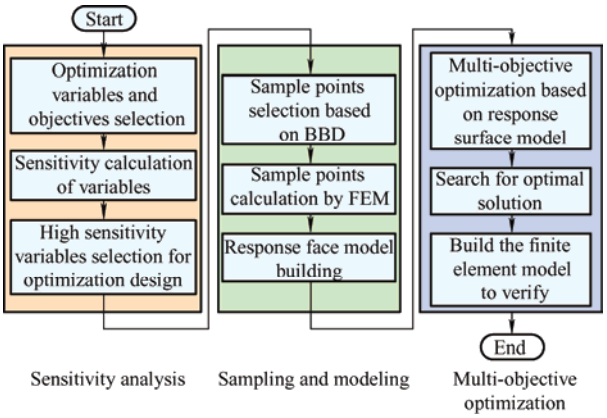

Fig. 10 Optimization process

4.1 Sensitivity analysis

Taking the proposed motor I as an example, its structure parameters are presented in Fig. 2, in which τ, g, and τ_m are fixed values. Meanwhile, L_{PM} and b_{s0}, H_{s0} and H_s have a specific quantitative relationship. Only one of them needs to be considered as the optimization variable. Therefore, there are five independent initial design variables, namely, b_{s0}, w_s, H_{PM}, e_1, and H_{s0}. Owing to the large number of variables, direct multi-objective optimization would increase the number of sample points to be calculated. However, some of the parameters negligibly influence motor performance. Therefore, the sensitivity of design variables should be analyzed before multi-objective optimization, which can effectively reduce the number of sample points. The sensitivity of design variables to optimization objectives is represented by the sensitivity index, and the sensitivity index can be expressed as

$$S_{n_i} = \frac{n_i \Delta f}{f \Delta n_i} \tag{21}$$

where n_i and f denote the optimization variable and optimization objective, respectively.

For the proposed motors, the optimization objectives are selected as average thrust force (TF_{avg}), thrust force ripple (TF_r), and power factor (PF), in which TF_{avg} and PF represent the forward optimization objectives, while TF_r denotes the negative optimization objective. TF_r is defined as

$$TF_r = \frac{TF_{\max} - TF_{\min}}{TF_{\text{avg}}} \times 100\% \tag{22}$$

where $TF_{\max}$ and $TF_{\min}$ represent the maximum and minimum values of thrust force, respectively.

According to Eq. (21), the sensitivity index of each design variable to the three optimization objectives can be calculated, as presented in Tab. 1. Taking the TF_{avg} sensitivity calculation process of b_{s0} as an example, the corresponding sensitivity values are calculated by simulating TF_{avg} under different b_{s0}, and then the average value is considered the sensitivity of b_{s0} to TF_{avg}. The calculation results are presented in Tab. 2. Tab. 1 indicates that there is no regularity in sensitivity of the variables to each optimization objective. Therefore, the sensitivity to the optimization objectives should be assessed by a comprehensive sensitivity index. Here, the comprehensive sensitivity index is given as

$$S_c = a_1 \left| S_{TF_{\text{avg}}} \right| + a_2 \left| S_{TF_r} \right| + a_3 \left| S_{PF} \right| \tag{23}$$

where a_1, a_2, and a_3 are the sensitivity coefficients of each optimization objective. The average thrust force is considered the performance index, which takes precedence over thrust force ripple and power factor, while the thrust force ripple and power factor are of the same importance. Therefore, the values of a_1, a_2, and a_3 are set as 0.5, 0.25, and 0.25, respectively. The comprehensive sensitivity of the variables is layered, and the comprehensive sensitivity value is considered the index of selecting the optimization variable. The higher the comprehensive sensitivity value, the greater the influence of the variable on the motor performance. For the proposed motor I, H_{PM} is categorized into the first level, and its comprehensive sensitivity is significantly higher than other variables. b_{s0} and e_1 are categorized into the second level, and finally w_s and H_{s0} are categorized into the third level. Therefore, the first and second level variables are selected as multi-objective optimization variables, namely, the three parameters of H_{PM}, b_{s0}, and e_1 are optimized. Similarly, for the proposed motor II, the results are similar to those of the proposed motor I and are not described herein.

Tab. 1 Sensitivity index calculation

Optimization objectives	Optimization variables				
	b_{s0}	w_s	H_{PM}	e_1	H_{s0}
TF_{avg}	–0.006	–0.021 5	0.245	0.017	0.022 5
TF_r	–0.051	–0.029	0.036	0.091	0.019
PF	0.071	0	0.395	–0.014	0.013 7
S_c	0.033 5	0.025 3	0.230	0.034 8	0.019 4

Tab. 2 TF_{avg} sensitivity index calculation with b_{s0}

Items	b_{s0}/mm				
	0	1	2	3	4
TF_{avg}/N	763.5	756.9	769.5	738.1	742.1
S_{bs0}	—	–0.009	0.004	–0.011	–0.007
$S_{TF_{\text{avg}}}$	(–0.009+0.004–0.011–0.007)/4=0.033 5				

4.2 Multi-objective optimization

In this study, the Box-Behnken design (BBD) was adopted to select sample points for the response surface model. The distribution of sample points in BBD can be presented in Fig. 11. Evidently, only 13 samples are required because there are three independent variables of the proposed DS-PPMVL motors. In the optimization process, the variation ranges of b_{s0}, H_{PM}, and e_1 are 0-4 mm, 1-4 mm, and 0.2-0.5, respectively. b_{s0} and H_{PM} determine the consumption of PM. The variation range of each variable is determined by the constraints of motor size parameters. Therefore, the sample points can be listed as

$$\begin{gathered}(b_{s0},H_{PM},e_1)=(0,1,0.35),(4,1,0.35),(0,4,0.35),\\(4,4,0.35),(0,2.5,0.2),(4,2.5,0.2),\\(0,2.5,0.5),(4,2.5,0.5),(2,1,0.2),\\(2,4,0.2),(2,1,0.5),(2,4,0.5)\\\text{and }(2,2.5,0.35)\end{gathered} \tag{24}$$

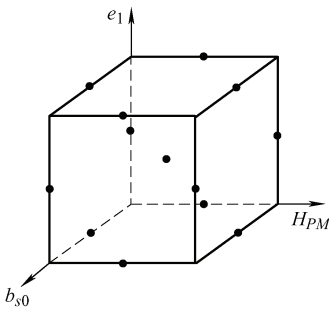

Fig. 11 Distribution of sample points in BBD

All the samples are calculated by FEM. Via parameter fitting, the second-order model is used for TF_{avg} and TF_r, while the linear model is adopted for PF. Taking the proposed motor I as an example, based on the FEM results, the response surface of each optimization objective of the proposed motors can be expressed as Eq. (25). The multiple correlation coefficients (R^2) are presented in Tab. 3. Notably, the closer R^2 is to 1, the higher the fitting accuracy. It can be inferred that all the values of R^2 are above 0.95. Therefore, the fitting models exhibit high correlation and optimal suitability.

$$\begin{cases}TF_{\text{avg}}=814.1-15.16b_{s0}+82.52H_{PM}-23.81e_1-\\\qquad 0.5b_{s0}H_{PM}+6.97b_{s0}e_1-34.25H_{PM}e_1-\\\qquad 15.26b_{s0}^2-124.99H_{PM}^2-86.16e_1^2\\TF_r=-12.9+1.977b_{s0}+2.4H_{PM}+112.89e_1+\\\qquad 0.08b_{s0}H_{PM}-1.67b_{s0}e_1-3.78H_{PM}e_1-\\\qquad 0.56b_{s0}^2+0.14H_{PM}^2-109.44e_1^2\\PF=0.573\,1+0.036\,2b_{s0}+0.168\,7H_{PM}-0.052\,5e_1\end{cases} \tag{25}$$

Tab. 3 Multiple correlation coefficients of proposed motors

R^2	Proposed motor I	Proposed motor II
TF_{avg}	0.99	1
TF_r	0.98	0.97
PF	0.96	0.96

Because the size parameters corresponding to the optimal solutions of the three optimization objectives are inconsistent, a compromise method is adopted to select the optimal solution. The relationship between the compromise objective and the three optimization objectives can be expressed as

$$Co=w_1TF_{\text{avg}}-w_2TF_r+w_3PF \tag{26}$$

where w_1, w_2, and w_3 represent the weight ratios of the optimization objectives. They satisfy $w_1+w_2+w_3=1$. In addition, the value of TF_r is negatively correlated with motor performance. Therefore, the coefficient of TF_r in Eq. (26) is negative. The weight ratios of TF_{avg}, TF_r, and PF are selected to be 0.6, 0.2, and 0.2, respectively. Taking TF_{avg} as an example, the results calculated by multi-objective optimization are presented in Figs. 12 and 13. The prediction results of TF_{avg} of the proposed motors can be found to be approximately 801.3 N and 874.8 N, respectively. The general optimization prediction results are presented in Tab. 4.

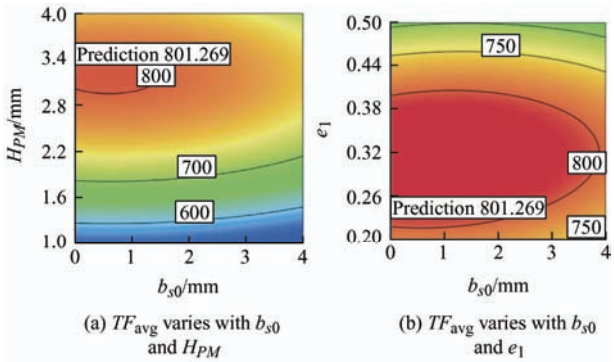

Fig. 12 Optimization results of TF_{avg} of proposed motor I

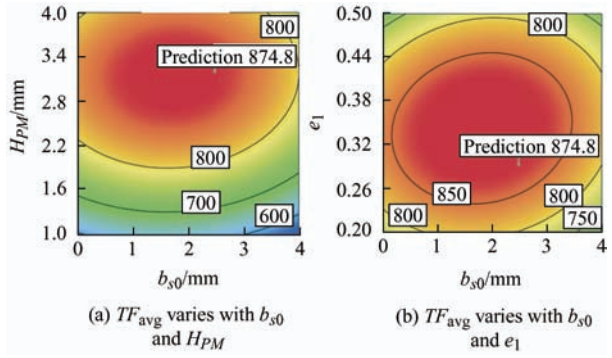

Fig. 13 Optimization results of TF_{avg} of proposed motor II

Tab. 4 Optimization prediction results

Parameter	Proposed motor I	Proposed motor II
b_{s0}/mm	0	2.48
H_{PM} /mm	3.2	3.2
e_1	0.22	0.29
TF_{avg}/N	801.4	874.8
TF_r (%)	13.2	11.5
PF	0.66	0.69

According to the aforementioned results, the structure parameters are applied to the motor models. The FEM prediction results of the proposed motors are presented in Figs. 14 and 15. For the proposed motor I, the values calculated by the FEM of TF_{avg}, TF_r, and PF are 784.6 N, 20.6% and 0.67, respectively. The error ratios of TF_{avg} and PF are approximately 2.1% and 1.5%; this implies that the TF_{avg} and PF results of multi-objective optimization agree well with those of FEM. Nevertheless, the TF_r of multi-objective optimization is significantly less than it of FEM. For the proposed motor II, the values calculated by FEM of TF_{avg}, TF_r, and PF are 848 N, 11.4% and 0.75, respectively. The result indicates that the errors between the multi-objective optimization and FEM of thrust force and thrust force ripple are also negligible. In summary, the designed response surface exhibits high fitting accuracy.

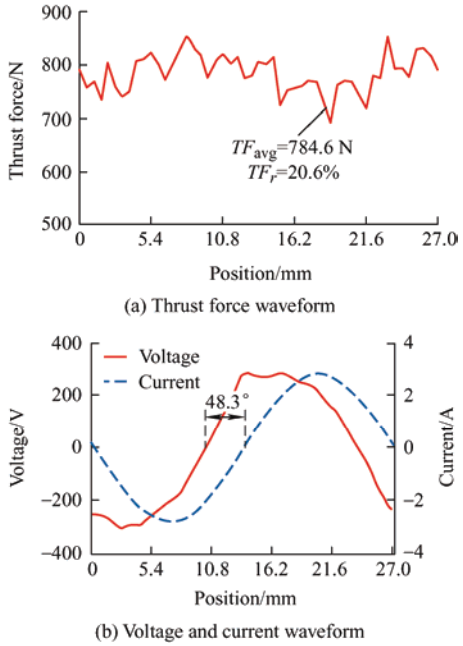

Fig. 14 FEM results of proposed motor I

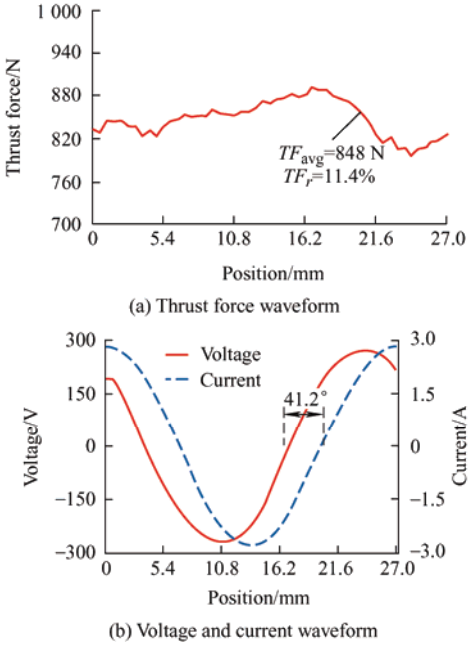

Fig. 15 FEM results of proposed motor II

5 Performance analysis

In this section, the electromagnetic performances are comprehensively compared among the two proposed motors and the existing one. The performances were calculated by time-step FEM simulation with movements in the mover. Some important parameters are presented in Tab. 5. Evidently, the proposed motors have a larger slot area and lesser consumption of PM than the existing alternatives.

Tab. 5 Motor parameters

Item	Motor I	Motor II	Existing
e_1	0.3	0.35	0.4
b_{s0}/mm	0	1	8
H_{PM} /mm	3.2	3.2	4.5
Area of slot/mm^2	266.4	266.4	216
Turns number per slot	102	102	84
Volume of PM/cm^3	162	162	190

5.1 No-load condition

Fig. 16 compares the back-EMFs and detent forces of the proposed motor I, proposed motor II, and existing motor. The fundamental amplitude values of the back-EMF of the three motors are 191 V, 206.6 V, and 169.2 V, respectively. It can be inferred that the back-EMFs of the proposed motors can be improved by 12.9% and 22.1% based on that of existing one, respectively. In addition, the peak-to-peak values of the detent force of the three motors are 125.7 N, 50.1 N, and 54.7 N, respectively. Evidently, the detent force of the proposed motor I is the largest, followed by that of the proposed motor II and the existing one. Therefore, the proposed motor II has merits both in terms of back-EMF and detent force.

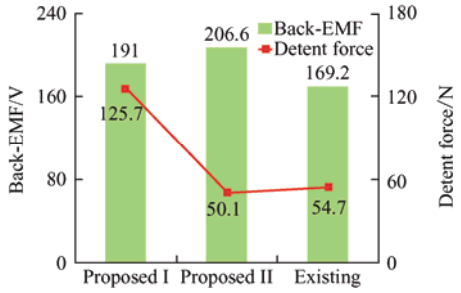

Fig. 16 Comparisons of back-EMFs and detent forces

5.2 Load condition

Important loading performance parameters, including thrust force, thrust force ripple, power factor, loss, and efficiency are compared herein. The comparison of the above performances is presented in Tab. 6. The average thrust force of the existing motor is 683.3 N, while those of the proposed motors are 784.6 N and 848 N. Therefore, the proposed motors provide higher thrust force in the case of less PM consumption. The thrust force ripples of the three motors are 20.6%, 11.4%, and 11.6%, respectively. The proposed motor II has the maximum thrust force and minimum thrust force ripple among the three motors. Fig. 17 depicts a comparison of the overload performances of the three motors. Evidently, the proposed motors share the same linear range, namely 0-6 A, while that of the existing alternative is in the range of 0-3 A. It primarily triggered by the saturation effect. When the rated current is 2 A, the proposed motors have three times overload capacity, while the existing motor is only 1.5 times. Therefore, the proposed motors exhibit better overload performance. In addition, the power factors of the three motors are compared in Tab. 6, which indicates that the power factor of the existing motor is the highest, followed by the proposed motor II, and then the proposed motor I.

Tab. 6 Performance comparison

Item	Motor I	Motor II	Existing
Thrust force/N	784.6	848.0	683.3
Thrust force ripple(%)	20.6	11.4	11.6
Power factor	0.67	0.75	0.82
Core loss/W	10.1	11.9	17.7
PM loss/W	1.55	1.46	0.015
Copper loss/W	169.5	169.5	139.6
Efficiency(%)	81.2	82.2	81.6

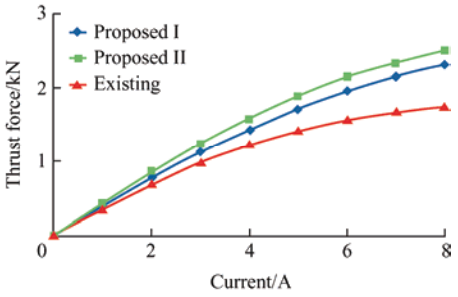

Fig. 17 Comparison of overload performance

In addition, it can be inferred that the copper loss of the proposed motors is higher than that of the existing one. Meanwhile, core losses of the proposed motors are smaller than those of the existing motor. Meanwhile, because the PMs of the proposed motors are adjacent to the air gap, and those of the existing motor are embedded in the iron core, the PM loss of the proposed motors is also larger than that of the existing one. However, the loss of PM accounts for the smallest proportion of the total loss. According to the output power and loss, the efficiencies of the proposed motor I, proposed motor II, and existing motor can be

calculated as 81.2%, 82.2%, and 81.6%, respectively. It should be explained that under the same electrical load, the proposed motor II exhibits the largest output thrust force, resulting in the largest output power. Although the loss is larger than the existing motor, the overall efficiency is the highest. Meanwhile, the output power of the proposed motor I is higher than that of the existing motor. However, its loss is higher than the existing motor, which implies that the efficiency is a litter lower than the existing motor.

6 Experimental verification

The existing DS-PPMVL motor has been processed. Owing to the similar structures and magnetic field analysis models of the proposed motors and existing motor, the prototype based on the existing motor can be utilized to verify the accuracy of motor design and analysis. The prototype and experimental setup are illustrated in Fig. 18. The experimental setup includes a prototype, dSPace 1005 controller, tension sensor, magnetic powder brake, connecting wire rope, and an oscilloscope. During the test, the magnetic powder brake was adopted as the load and connected with the prototype using a wire rope. The tension sensor was installed on the wire rope to measure the thrust force. It should be noted that the length of the air gap is 1.5 mm instead of 1 mm of the original design owing to processing error. To verify the accuracy of the aforementioned design, the FEM air gap length of the existing motor has been adjusted to 1.5 mm. Meanwhile, owing to the limitation of stator length, the experimental speed is less than 1 m/s.

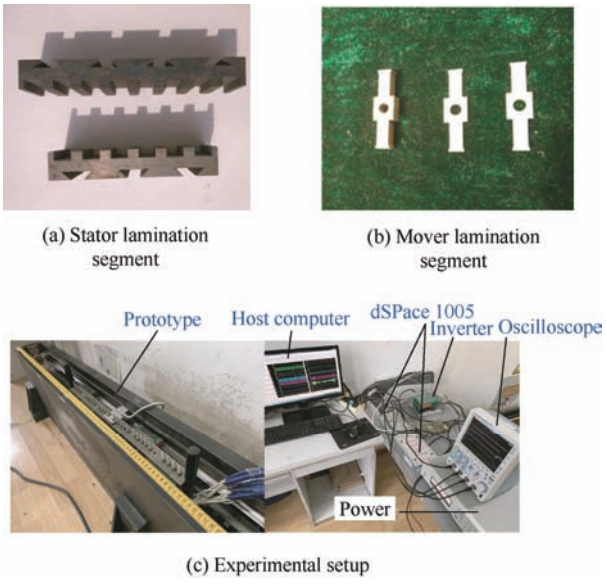

(a) Stator lamination segment

(b) Mover lamination segment

(c) Experimental setup

Fig. 18 Prototype of the existing motor

Fig. 19a presents the back-EMF of experimental measured by 0.35 m/s. The waveforms of back-EMF are sinusoidal and symmetrical, while the amplitude is approximately 39 V, which agrees well with FEM results, as illustrated in Fig. 19b. Fig. 20 compares the static thrust forces between the experimental and FEM results. The thrust force varies linearly with the current owing to the unsaturation under low-load conditions. The maximum difference of thrust forces between FEM and experimental is approximately 5.7%.

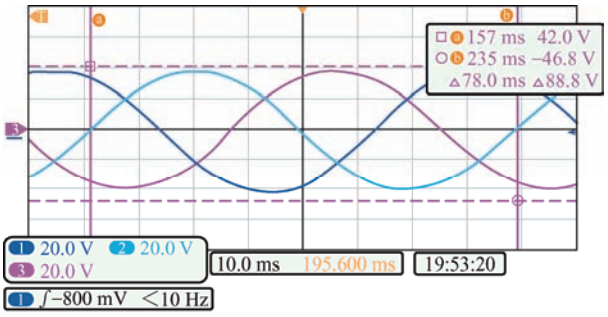

(a) Measured(20 V/div)

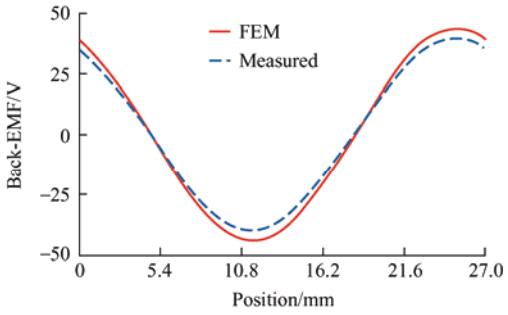

(b) Comparison

Fig. 19 Back-EMF at 0.35 m/s

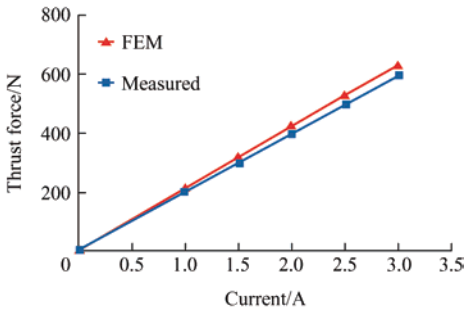

Fig. 20 Simulated and measured thrust forces versus current

7 Conclusions

Two DS-PPMVL motors with asymmetric CP PM structure were developed in this study. Based on the analytical and experimental investigations, the

following conclusions can be drawn.

(1) The operation principle was analyzed considering the proposed motor I as an example. The analysis of the thrust force mechanism revealed that the low-order MMF harmonics significantly influence the performance.

(2) The relationship between the proposed motors and the existing motor was clarified. A BBM was adopted to develop the unified analytical model. Based on the unified analytical model, the air-gap flux density of the proposed motor I was calculated, and the results agreed well with the FEM results.

(3) By analyzing the difference in MMF, the internal performance improvement mechanism with the CP PM structure was elucidated.

(4) To improve the optimization efficiency, the multi-objective optimization method was adopted and the global optimal solutions were determined.

(5) Compared with the existing motor, the proposed motors have the merits of larger slot area, less PM usage, higher thrust forces, and better overload performance. Therefore, the utilization rate of the PM can be significantly improved, which is suitable for the long-stroke applications. However, certain demerits also exist in the proposed motors, such as lower power factor, higher copper and PM losses.

Finally, the experiments based on the prototype were completed. All the experiment results agreed well with FEM results, thereby verifying the effectiveness of the theoretical analysis.

References

[1] W Xu, X Xiao, G Du, et al. Comprehensive efficiency optimization of linear induction motors for urban transit. *IEEE Transactions on Vehicular Technology*, 2020, 69(1): 131-139.

[2] S Qiu, W Zhao, C Zhang, et al. A novel structure of tubular staggered transverse-flux permanent-magnet linear generator for wave energy conversion. *IEEE Transactions on Energy Conversion*, 2022, 37(1): 24-35.

[3] M Zhao, Y Wei, H Yang, et al. Development and analysis of novel flux-switching transverse-flux permanent magnet linear machine. *IEEE Transactions on Industrial Electronics*, 2019, 66(6): 4923-4933.

[4] X Zhu, C H T Lee, C C Chan, et al. Overview of flux-modulation machines based on flux-modulation principle: Topology, theory, and development prospects. *IEEE Transactions on Transportation Electrification*, 2020, 6(2): 612-624.

[5] P Han, M Cheng, X Zhu, et al. Analytical analysis and performance characterization of brushless doubly fed induction machines based on general air-gap field modulation theory. *Chinese Journal of Electrical Engineering*, 2021, 7(3): 4-19.

[6] I Eguren, G Almandoz, A Egea, et al. Linear machines for long stroke applications: A review. *IEEE Access*, 2020, 8: 3960-3979.

[7] R Cao, Y Jin, M Lu, et al. Quantitative comparison of linear flux-switching permanent magnet motor with linear induction motor for electromagnetic launch system. *IEEE Transactions on Industrial Electronics*, 2018, 65(9): 7569-7578.

[8] Q Lu, Y Yao, J Shi, et al. Design and performance investigation of novel linear switched flux PM machines. *IEEE Transactions on Industrial Applications*, 2017, 53(5): 4590-4602.

[9] W Zhao, J Zhu, J Ji, et al. Improvement of power factor in a double-side linear flux-modulation permanent-magnet motor for long stroke applications. *IEEE Transactions on Industrial Electronics*, 2019, 66(5): 3391-3400.

[10] W Zhao, A Ma, J Ji, et al. Multiobjective optimization of a double-side linear vernier PM motor using response surface method and differential evolution. *IEEE Transactions on Industrial Electronics*, 2020, 67(1): 80-90.

[11] J Li, K Wang, C Liu. Comparative study of consequent-pole and hybrid-pole permanent magnet machines. *IEEE Transactions on Energy Conversion*, 2019, 34(2): 701-711.

[12] W Ullah, F Khan, M Umair. Optimal rotor poles and structure for design of consequent pole permanent magnet flux switching machine. *Chinese Journal of Electrical Engineering*, 2021, 7(1): 118-127.

[13] S Cai, Z Q Zhu, C Wang, et al. A novel fractional slot non-overlapping winding hybrid excited machine with consequent-pole PM rotor. *IEEE Transactions on Energy Conversion*, 2020, 35(3): 1628-1637.

[14] H Yang, Z Q Zhu, H Lin, et al. Analysis of consequent-pole flux reversal permanent magnet machine with biased flux modulation theory. *IEEE Transactions on Industrial Electronics*, 2020, 67(3): 2107-2121.

[15] H Yang, Y Li, H Lin, et al. Principle investigation and performance comparison of consequent-pole switched flux PM machines. *IEEE Transactions on Transportation Electrification*, 2021, 7(2): 766-778.

[16] Y Zhou, R Qu, C Shi, et al. Analysis of thrust performance of a dual-mover linear vernier machine with horizontal-magnetized PM arrays. *IEEE Transactions on Energy Conversion*, 2018, 33(4): 2143-2152.

[17] X Zhang, P Fu, Y Ma, et al. No-load iron loss model for a fractional-slot surface-mounted permanent magnet motor based on magnetic field analytical calculation. *Chinese Journal of Electrical Engineering*, 2018, 4(4): 71-79.

[18] P Wang, W Hua, G Zhang, et al. Principle of flux-switching PM machine by magnetic field modulation theory part I: Back-EMF generation. *IEEE Transactions on Industrial Electronics*, 2022, 69(3): 2370-2379.

[19] P Wang, W Hua, G Zhang, et al. Principle of flux-switching PM machine by magnetic field modulation theory part II: Electromagnetic torque generation. *IEEE Transactions on Industrial Electronics*, 2022, 69(3): 2437-2446.

[20] W Wang, J Zhao, Y Zhou, et al. New optimization design method for a double secondary linear motor based on R-DNN modeling method and MCS optimization algorithm. *Chinese Journal of Electrical Engineering*, 2020, 6(3): 98-105.

Jinghua Ji received B.S., M.S., and Ph.D. degrees in Electrical Engineering from Jiangsu University, Zhenjiang, China, in 2000, 2003, and 2009, respectively. Since 2000, she has been with the School of Electrical and Information Engineering, Jiangsu University, where she is currently a Professor. From 2013 to 2014, she was a Visiting Scholar with the Department of Electronic and Electrical Engineering, University of Sheffield, Sheffield, UK. Her areas of interest include motor design and electromagnetic field computation. She has authored and co-authored over 100 technical papers in these areas.

Xuhui Zhu received the B.Sc. degree and Ph.D. degree in Electrical Engineering from Jiangsu University, Zhenjiang, China, in 2015 and 2021, respectively.

He has been a Lecturer with Nantong University, Nantong, China, since Dec. 2021. He is currently a Postdoctoral Research Fellow with the School Electrical and Electronic Engineering, Nanyang Technological University, Singapore. His research interests include flux-modulation motor design, electromagnetic field computation and motor control.

Hongyu Tang received the B.Sc. degree in Electrical Engineering from Jiangsu University of Science and Technology, Zhenjiang, China, in 1999, and the M.Sc. degree in Electrical Engineering from Jiangsu University, Zhenjiang, China, in 2005.

He has been with Zhenjiang College since 1999, where he is currently a Professor with the School of Electrical and Information. His current research interests include analysis and control of permanent-magnet motor drive systems.

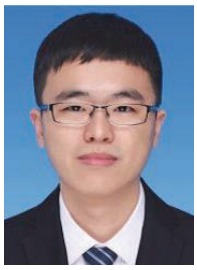

Liang Xu received the B.Sc. degree in Electrical Engineering and Automation from Soochow University, Suzhou, China, in 2011, the M.Sc. degree in Power Electronics and Power Drives from Jiangsu University, Zhenjiang, China, in 2014, and the Ph.D. degree in Control Science and Engineering from Jiangsu University, Zhenjiang, China, in 2017. Since 2017, he has been with Jiangsu University, where he is currently an Associate Professor with the School of Electrical and Information Engineering. Since 2021, he has been serving as a Postdoctoral Fellow with the Department of Electrical Engineering, The Hong Kong Polytechnic University, under Hong Kong Scholars Program. His areas of interest include electrical machines and drives.

Wenxiang Zhao (M'08-SM'14) received the B.Sc. and M.Sc. degrees in Electrical Engineering from Jiangsu University, Zhenjiang, China, in 1999 and 2003, respectively, and the Ph.D. degree in Electrical Engineering from Southeast University, Nanjing, China, in 2010.

He has been with Jiangsu University since 2003, where he is currently a Professor with the School of Electrical and Information Engineering. From 2008 to 2009, he was a Research Assistant with the Department of Electrical and Electronic Engineering, The University of Hong Kong, Hong Kong, China. From 2013 to 2014, he was a Visiting Professor with the Department of Electronic and Electrical Engineering, University of Sheffield, Sheffield, UK. He has authored and co-authored over 150 papers published in various IEEE Transactions. His current research interests include electric machine design, modeling, fault analysis, and intelligent control.